Student thesis: Master thesis TU Delft
Supervisors: M.E. Donselaar, J. Bruining and K.H.A.A. Wolf

Spontaneous Combustion of the Kimmeridge Clay Formation Oil Shale; from Geology to Modelling

Jaya M. Kisoensingh

18th March 2009

Abstract

Burning oil shales contribute to CO_2 emissions. The spatial distribution pattern shows that these fires occur in areas with moderate or dry climates. This paper investigates the mechanism behind the burning oil shales. The first part includes an overview of the geological setting, fieldwork results and petrophysical analyses. Based on these settings, we defined a horizontal fractured structure above and below the shale beds and vertical fractures with spacing varying from 10–30 cm. The matrix in between is oil shale with a kerogen content of 35 % up to 70 %. The oil shale contains lenses of pyrite. Several dynamic models, based on this fractured oil shale structure, have been developed to illustrate aspects leading to enhancements or extinction of oil shale fires. Natural convection supplies air (oxygen) to sustain combustion. Air can penetrate into the matrix, mainly to the highly fractured structure, to react with fuel. The presence of oxidising pyrite may trigger the fire. Favourable conditions for oil shale fires are dryness, mostly during the summer, and a heat source.

1 Introduction

Spontaneous combustion of oil shales is repeatedly recorded in deposits outcropping around the world. The spatial distribution of oil shale fires indicates that the fires occur in areas with moderate or dry climates. These fires have great resemblance with the subsurface coal seam fires[14] occurring across the world and both contribute to the global CO_2-emission. The scale of burning shale formations can be relatively large. For example, the Hatrurim Formation (Israel) shows shale fires over an area of circa 250 km^2, burning at (800–1200 K)[8]. The combustion has environmental consequences due to emission of sulphuric oxides and other greenhouse gases. Although there have been several reports of burning oil shale, the phenomenon of shale fires is hardly investigated and therefore relatively unknown. It is not clear whether or not the combustion of the Kimmeridge oil shale fire was spontaneous[12]. However, spontaneous ignition is likely.

The aim of this research is to explain the phenomenon of the burning oil shales by investigating the temperature distribution, oxygen flows paths and flow rates. In order to investigate spontaneous ignition of oil shales, the oil shale or Blackstone in the Kimmeridge Clay Formation has been studied. The Kimmeridge oil shale has been observed to be on fire for several years in 1826[1] , in 1973/1974[2] and relatively recent

for 3 months in 2000[10]. The Blackstone was chosen for this research because of the known irregular spontaneous combustion occurrences at Dorset coast, their accessibility, good exposure and abundant available geological literature.

This article starts with methods and data acquisition (see section 2, where the used procedures, methods and data are briefly explained. Next a geological overview is given in section 3. Section 4 provides information about field observations and geological data. Section 5 gives an overview of the input data, which were obtained by experiments done by Lars van Zelm (2008) during his B.Sc. thesis. Section 6 explains the physical model, which is based on the field observations, and methods. The results and discussion follow in section 7.

2 Methods and data acquisition

Literature research was done in order to gain data and information on spontaneous ignition of oil shales generally and specifically the burning oil shales of the Kimmeridge Clay Formation[1, 2, 6, 15, 5, 8, 12]. In addition, geological information on the Kimmeridge Clay Formation was reviewed[1, 3, 4, 9, 7, 10, 11, 12]. We went on a field trip to do visual observations, take samples, do measurements and take scaled pictures of the outcrop. Resistivity and electromagnetic measurements were done on the top of the cliff. Section 4 discusses and shows the results of these measurements. The other field parameters such as orientation, fracture density, dimensions of the Blackstone layer were measured during the fieldwork[1]. Literature data of the mineral components[3, 10] were used to compare the the outcomes of our research on mineral components. Lab experiments [2] on samples of the Blackstone were performed. The results before and after thermal treatment by using XRD, XRF, thins sections, Ruska permeameter and the Ultrapycnometer provided an overview on mineral content, porosity and permeability. Using parameters obtained from fieldwork, lab experiments and literature, we the modelled the oxygen flow necessary for combustion, calculated the flow velocity and temperature distribution.

3 Geology

The Kimmeridge Clay Formation is an argillaceous lithostratigraphical unit which, in South Dorset (England)[3], ranges from 300 m to more than 500 m in thickness[3]. The Kimmeridge Clay Formation is of late Jurassic (155.7–150.8 Ma) age and is made up almost entirely of soft mudstone, calcareous mudstone and kerogen-rich mudstone (bituminous mudstone and oil shales)[3]. These sediments are dark grey to black and contain several thin (less than 1 m) layers of grey dolomitic siltstone and light grey to white cocolithic limestone. The biogenic input (primarily cocoliths) of this formation is very high. The Kimmeridge Clay Formation shows Milankovitch Band climatic cyclicity[7]. The cyclicity is defined by measuring parameters such as magnetic susceptibility or the organic matter content of the sediments[9]. Central to arguments about the Kimmeridge Clay Formation environment is the role of productivity and/or preservation in the deposition of the organic matter. Research[7] shows that the increased total organic carbon (TOC) values res-

[1] See section 4

[2] See section 5

[3] See location map in appendix

ult from increased preservation rather than productivity. The mechanism was the relative upward movement of the lower euxinic water mass into the photic zone. This greatly reduced the possibility of organic matter being oxidised during its descent through the water column. Therefore significant quantities of carbohydrates reached the sea bed and were subsequently preserved by sulphurization and result in a significantly increased carbon sequestration to the sea-floor sediment. The formation is thus deposited in a deep marine environment with both restricted circulation and variable oxygen content, below the wave-base, so sedimentation of fine grains and thin layers was possible[3, 10, 6, 7]. In addition the high sedimentation rate (88.452 m /million years) contributed to the high organic content[4]. Several large faults were observed. In late Jurassic and early Cretaceous times this was an area of extension, being pulled apart before the formation of the Atlantic. The faults at Kimmeridge are all extensional and of this age[11]. The phase of extensional faulting culminated in about the middle of the Cretaceous as the North Atlantic began to open (the opening of the North Atlantic started in about the Valanginian to Hauterivian). This phase of faulting is known as Late Kimmerian or Late Cimmerian. Much later, in the Tertiary, there was compression, as the African Plate impacted on the European Plate. The Alps and Pyrenees were formed. The major orogeny is usually referred to as the Alpine Orogeny, but it extended over a time period from about Eocene to Miocene. In Dorset this compressional phase formed major anticlines (actually over deep reactivated faults). The small anticline at Kimmeridge has not been specifically dated, but probably corresponds to this comparessional phase[11, 10]. The Kimmeridge Clay Formation is best known for its potential as source rock providing over 90 % of the Northern North Sea oil.

3.1 The Blackstone

The Kimmeridge oil shale is a black mudstone with a kerogen content up to 70 %. Petrochemical analyses of the oil shale show around 20–50 % clay minerals, 10–25 % calcium carbonate and 10–20 % quartz as the major sedimentary components[3]. The blackstone also contains a remarkable amount of pyrite. The pyrite nodules are a result of sulphate-reducing bacteria living on the organic matter of the oil shale shortly after deposition and reducing the sulphate of sea-water to sulphide. During compaction and diagnesis it reacted with available iron to produce the ferrous sulphide (pyrite = FeS_2). In the field the Blackstone has a high vertical fracture density, varying from 20–40 cm distance. These joints are the result of gravity forces and erosion. They can be followed 1 m into the cliff. The white surfaces of vein-calcite on joints in the black oil shale are a famous feature of the Blackstone, giving it its characteristic black and white appearance[11].

4 Field observations, measurements and interpretations

The Blackstone is best seen at Clavell's Hard, East of Kimmeridge Bay. Here the Blackstone is at a accessible height from the coastal plain. The formation dips 10° to the East. We observed a black layer with a more or less constant thickness of circa 0.86 m The layer shows many vertical sub-parallel fractures. The fractures with a width of 2–3 cm occur at intervals of approximately 0.3 m from each other and can be followed

more than 0.7 m into the wall. The Blackstone is bounded above and below by sharp erosional surfaces.

These observations are interpreted and implemented in the in the combustion model which is discussed in section 6. The observations are interpreted as follows; Because of the highly fractured pattern of the Blackstone, we assume that the oxygen for combustion was supplied mainly via fractures. Large faults were also observed in the outcrop, although not in the Blackstone layer and therefore not taken into account in the model. Another potential way of oxygen supply could be via tunnels. The cliff has been exploited in the first half of the 20$^{\text{th}}$ century as a domestic fuel source. There might still be tunnels present in the area, but their locations, orientation and dimensions are unknown due to cliff erosion and the second world war.

The fire of 1973–1974 mentioned by Cole took place 6–8 m below the top of the cliff. The oxidation of pyrite ignited the shale[2]. The area still has a red brownish colour due to oxidation. The thermal area has a thickness of 6 m at the centre of the zone and narrows down to 3 m at the edges. Erosion over the past decades removed parts of the original cliff settings. Hence, depth of the original fire cannot be traced from this place. In addition, no evidence is found on the coastal plain because burnt pieces have been washed away by the tide.

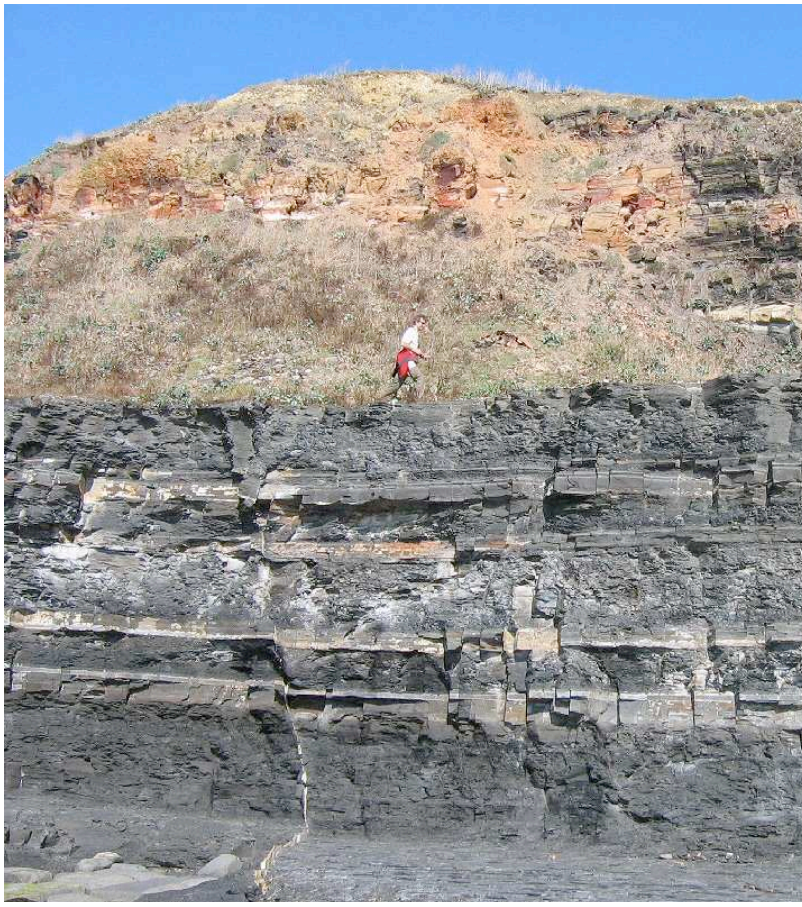

Figure 1: The burnt cliff

4.1 Geophysical field exploration

The Kimmeridge clays and carbonate richer inter-strata consist mostly of low resistivity rocks (<ca. 75 Ω m). The thin limestone bands are higher resistivity zones. Clay minerals such as Kaolinite and Montmorillonite disintegrate starting at 690 °C. At higher temperatures, up

to 970 °C, illite follow[13]. Hence, the baked rock has very high resistivity characteristics (>ca. 1000 Ωm) and should give a sharp contrast with surrounding clays. In addition, based on resistivity, highly porous zones, such as caverns and large open fault systems can be detected. The resistivity measurements can thus provide us with evidence of larger open faults or fault patterns. A low dip (<5°) in East direction of the surface layer at the top of the cliff, facilitates the placing of he electrodes. We used two methods at the top of the cliff, above the burnt zone. (1) Electrical methods (using STING): We shot three lines; two of them were parallel and one was perpendicular to the cliff edge. The lines consisted of 84 electrodes, which were placed at a distance of 1 m. In order to reduce the influence of salty air, we placed the lines at least 20 m away from the cliff head. The measurements were based on the Schlumberger Inverse and Dipole-Dipole methods. We processed the data by inversion followed by conversion to 2D-sections. (2) Time-domain electromagnetic techniques (using TEMFAST): This technique is used to determine the electrical conductivity of the soil at a depth up to ca 25 m. We did five measurements; each in square zones of 25×25 m. Three of them covered the area of the Induced Resistivity measurements. The data of these series are unfortunately corrupted and have to be recovered. They are not used for interpretation.

4.2 Results

Measurements of both methods, Schlumberger Inverse and Dipole-Dipole, show in all lines a very low resistivity near the surface (see appendix). This is due to the relatively wet top soils and the continuous supply of salt by the sea wind. Especially the measurements of line 1 and 2 express this behaviour. Generally, the resistivity increases with depth. The inverted Schlumberger image of line 1 shows an increase in resistivity to the surface in the southward direction. This agrees with the dipping of the bedding. Line 3 shows the dipping of the beds in westward direction as well. All the inverted images show spots of high resistivity. They can be the results of either the presence of baked rock of combusted shales or an old tunnel. The resolution of the images is low and the results do not provide evidence for existing faults or fault patterns. Only line 3 gives possible proof for oxidation and combustion deeper into the cliff. If we assume that the higher resistivity spots are relics of shale fires, then the maximum depth of penetration should be about 20 m into the cliff.

5 Experimental results

Following the petrological and petrophysical results of Cox and Gallois and West[3, 11], the rock texture, structure and mineral content of the Blackstone was investigated by Zelm van[16]. His results before and after thermal treatment by using XRD, XRF, thins sections, Ruska permeameter and the Ultrapycnometer provided an overview on mineral content, porosity and permeability. Data end methodology follow in the apendixes.

5.1 Mineral composition

The results of the XRF analysis matches with the mineral composition found in literature [3, 4, 10]. Organic matter, clay, quartz and calcite are present in significant amounts. The amount of organic material decreases with temperature, due to combustion of the kerogen. Heat resistant

Table 1: the mineral content by the XRF analysis of an in-situ sample

Contents	Mole (%)	Weight (%)	Volume (%)
Kerogen	24	13	32
Calcite	39	40	32
Quartz	26	16	14
Pyrite	$4 \cdot 10^{-4}$	$4 \cdot 10^{-4}$	$2 \cdot 10^{-2}$
Clay	11	31	21.98
Total organic content		30 % –50 %	

Table 2: Porosity % at different temperatures

0	20 °C	300 °C	600 °C	900 °C	1000 °C
Average	4.11	10.67	46.40	63.23	64.95
St. dev.	1.74	0.82	1.37	0.67	0.95
N	40	10	10	10	10

minerals such as quart, anhydrite and feldspars dominate the mineral composition at high temperatures.

5.2 Porosity

The averaged in-situ porosity (at a temperature of 20 °C) of the samples is 4.11 %. The test results show a relatively high standard deviation due to the large variety of brittle fractures in the sample. Thermal fractures are due to the heating process. The porosity increases, as expected, with temperature. The increase of the matrix porosity at 300 °C can be explained by the combination of gasification of kerogen and the forming of tar from the original material. Both naturally occurring processes have opposite effect on the effective pore space of the samples. The steepest increase is between 300 °C and 600 °C. This increase is due to combustion of all organic matter. The porosity measured at 900 °C and 1000 °C are rather constant, with a small standard deviation. The appendix contains a graph of the porosity as a function of the temperature.

Table 3: Permeability[mD] at different temperatures

	20 °C	300 °C	600 °C	900 °C	1000 °C
Average	299	244	437	268	582
St.dev	225	210	137	31	96
N	20	12	4	8	3
Ave samples	412	382	1051	320	712
N (all)	20	12	9	10	6

Table 4: Input parameters used for modelling

Physical quantity	Symbol	Value	Unit
Thermal expansion coefficient	β	1.092×10^{-3}	$^1/_{\mathrm{K}}$
Acceleration due to gravity	g	9.81	$\mathrm{m/s^2}$
Fluid density	ρ_f	1.185	$\mathrm{kg/m^3}$
Specific heat	C_f	1007.5	$^{\mathrm{kg}}/_{\mathrm{J\,K}}$
Rock thermal conductivity	λ	2	$^{\mathrm{W}}/_{\mathrm{m\,K}}$
Viscosity	μ	1.87×10^{-05}	$^{\mathrm{kg}}/_{\mathrm{m\,s}}$
Reference permeabilty	κ	10^{-9}	$\mathrm{m^2}$
Fracture width		2	cm

5.3 Permeability

The results of the Ruska permeameter show relatively large variations for all samples per temperature. The cores needed to be tightly fixed by rubber sleeves. However, there was still some damage done, which led to high permeability values. The results of 900 °C can be explained by clogging effects of carbon rich remnants of the former kerogen matter. The general behaviour of the permeability shows an increase with temperature from ca. 300 mD to ca. 600 mD. (See appendix)

6 Modelling the oil shale fires

6.1 Physical model

We consider a highly porous horizontal layer, with a height (H) and length (L). This layer is bounded above and below by a sharp erosional surface. The layer contains vertical fractures

with a spacing of 25–30 cm. The permeability of these fractures is very high with respect to the already highly porous matrix. The air flow is therefore modelled solely through the fractures. The oxygen flow pattern through the fractures result in a ⊐-shaped model. The inlet is considered to be the horizontal wedge below the matrix and the outlet is the horizontal wedge above the matrix. A vertical fracture (every 25–30 cm) connects these two fractures with each other, which lead to a very permeable system.

Heat is generated by a heat source, as a result of the exothermal reaction for oxidation pyrite. The amount that reacts depends on the oxygen supply through the layer. We assume a steady state air flow. The motion is described by Darcy's law with a source term proportional to the density gradient. The mass conservation laws were added to Darcy's law to describe the diffusion and natural convection processes in the porous medium. The density varies with temperature (the Elder problem) and therefore the density cannot considered to be constant. However, we use Boussinesq approximation which considers density variations only when they contribute directly to the fluid/gas motion. The heat equation however, is used in a form to describe transient flows. The equation considers heat transport by natural convection, thermal diffusion and a source term.

6.2 Formulation

Continuity equation

$$\frac{\partial \rho}{\partial t} + \frac{\partial \left(\rho U_x\right)}{\partial X} + \frac{\partial \left(\rho U_z\right)}{\partial Z} = 0$$

We consider ρ to be constant, so the continuity equation can be simplified.

$$\frac{\partial \left(U_x\right)}{\partial X} + \frac{\partial \left(U_z\right)}{\partial Z} = 0 \tag{1}$$

Darcy's law in horizontal and vertical direction:

$$U_x = -\frac{\kappa}{\mu}\frac{\partial P}{\partial X} \tag{2}$$

$$U_z = -\frac{\kappa}{\mu}\left(\frac{\partial P}{\partial Z} + \rho g\right) \tag{3}$$

Differentiation of equation (2) to Z and equation (3) to X, followed by subtracting these two equations from each other, leads to elimination of P.

$$\frac{\partial U_z}{\partial X} - \frac{\partial U_x}{\partial Z} = -\frac{\kappa}{\mu}\rho g \beta \frac{\partial T}{\partial X} \tag{4}$$

The heat equation

$$\begin{aligned} \rho_m C_m \frac{\partial T}{\partial t} + \rho_f C_f \left(\frac{\partial U_x T}{\partial X} + \frac{\partial U_z T}{\partial Z}\right) \\ = \lambda \left(\frac{\partial^2 T}{\partial X^2} + \frac{\partial^2 T}{\partial Z^2}\right) \end{aligned} \tag{5}$$

where $\rho_f C_f$ is the heat capacity of the gas and λ is the thermal conductivity of the oil shale layer.

Equation (4) takes only the density dependence on temperature (Boussinesq approximation) is taken into account. As a driving force flow we approximate temperature dependence of the density with a linear expansion.

$$\Delta\rho = \rho - \rho_0 = \frac{(\rho_s - \rho_0)}{T_s - T_0}(T - T_0)$$

$$\beta = \frac{1}{\rho}\frac{\partial \rho}{\partial T}$$

$$\Delta\rho = \rho\beta(T - T_0)$$

where $\beta = -\frac{1}{T}$ is the thermal expansion coefficient based on the ideal gas law.

6.3 Equations in dimensionless form

We define:

$$U_x = -\frac{\partial \psi}{\partial Z} \tag{6}$$

$$U_z = \frac{\partial \psi}{\partial X} \tag{7}$$

$$\frac{\lambda}{\rho_f C_f} = \chi \tag{8}$$

Substituting equation (6) and (7) into equation (4) leads to:

$$\frac{\partial}{\partial X}\frac{\partial \psi}{\partial X} + \frac{\partial}{\partial Z}\frac{\partial \psi}{\partial Z} = -\frac{\kappa}{\mu}\rho g \beta \frac{\partial T}{\partial X} \tag{9}$$

Substituting equation (6), (7) and (8) into the heat equation results in:

$$-\left(\frac{\partial \psi}{\partial Z}\frac{\partial T}{\partial X}\right) + \left(\frac{\partial \psi}{\partial X}\frac{\partial T}{\partial Z}\right) = \chi\left(\frac{\partial^2 T}{\partial X^2} + \frac{\partial^2 T}{\partial Z^2}\right) \tag{10}$$

In order to write equation (9) and (10) in dimensionless form, we define:

$$X = X_D L \qquad Z = Z_D L$$

$$\psi = \psi_D \psi_R \qquad T = T_D T_R$$

$$Gr = -\frac{\kappa}{\mu}\rho g \beta t_R \frac{L}{\psi_R} \qquad Pr = \frac{\psi_R}{\chi}$$

Dimensionless form of equations (9) and (10):

$$\frac{\partial^2 \psi_D}{\partial X_D^2} + \frac{\partial^2 \psi_D}{\partial Z_D^2} = Gr \frac{\partial T_D}{\partial X_D} \tag{11}$$

$$\left(\frac{\partial \psi_D}{\partial X_D}\frac{\partial T_D}{\partial Z_D}\right) - \left(\frac{\partial T_D}{\partial X_D}\frac{\partial \psi_D}{\partial Z_D}\right) = \frac{1}{Pr}\left(\frac{\partial^2 T_D}{\partial X_D^2} + \frac{\partial^2 T_D}{\partial Z_D^2}\right) \tag{12}$$

6.4 Boundaries conditions and solution procedure

The pressure boundaries at the in and outlet are atmospheric. The pressure at the inlet is however, higher than at the outlet. This due to the thickness (P = ρgh, where h is the thickness) of the oil shale.

The initial boundary temperature at in and outlet is 400 K. The source temperature is caused by the exothermic reaction of pyrite and oxygen. The spontaneous combustion of pyrite releases heat. Considering the heat coefficient of the blackstone, a source temperature up to 800 K can be obtained[1]. Oxidation of pyrite: $FeS_2 + O_2 \rightarrow Fe_2O_3 + SO_2$

Equations (11) and (12) are solved using the finite volume method approach. Simulations are run using COMSOL Multiphysics/Earth Science Module.

6.5 Heat transfer by conduction and diffusion

The mathematical model for heat transfer by conduction is given by the following version of the heat equation

$$\rho c_p \frac{\partial T}{\partial t} - \nabla(K \nabla T) = (kreac \cdot c \cdot c_2) \exp \frac{-E}{RT}$$

where, K = thermal conductivity and kreac = reaction rate

The generic diffusion equation has the same structure as the heat equation. We have two diffusion equations (for the oxygen and for the air). The diffusion of the matrix and the air (oxygen) is governed by

$$\frac{\partial c}{\partial t} + \nabla(-D \nabla c) = -(kreac \cdot c \cdot c_2) \exp \frac{-E}{RT}$$

where, D = the diffusion coefficient, which is different for the matrix and air. c and c_2 are respectively the concentrations of the solid and oxygen.

Modelling these three equations, with the three unknown (T,c,c_2) will lead to the heat transfer as a function of the oxygen concentration. This indicates the amount of air needed for combustion.

7 Results and discussion

Heating effects in samples can be recognised by dehydroxylised clay minerals and oxidised organic components. These symptoms occur when samples are heated to temperatures of 500 K and higher. We assume that fires will not occur in cases for which the temperature fall below 450 K.

The used input parameters are summarised in table 4. Figure 4 shows the results of the temperature distribution. Large changes in temperature are characterised by large colour variations (from blue to dark red). The temperature is relatively low at the inflow. The air progressively heats up as it approaches the heat source. Hot air rises up in the vertical fracture and flows out via the upper horizontal fracture. As the air approaches the 'end' of the fracture, it cools down. The black arrows indicate the flow direction. The horizontal velocity in the lower horizontal fracture reaches 1×10^{-4} m/s. The upper horizontal velocity reaches the same velocity, but in opposite direction. This explains the minus (-) sign. The velocity in vertical direction reaches 5×10^{-5} m/s in the vertical fracture. Figure 2 and 3 show respectively the Darcy velocity in the horizontal and vertical direction.

From figure 2 and 3 we obtain a velocity of 4–9 m/day. Taking the dimensions of the surface of the exposed burnt cliff into account and assuming that the blackstone burnt up to 1 m into the cliff leads to burnt oil in 48 m^3 matrix. This means that the total oxidation of the cliff could take place in 8 days. In reality the cliff burnt for longer then 12 months. This supports the outcomes of the conduction and diffusion model, which indicate that the oxidation of the cliffs are limited by the reaction rate. Scenarios with variable fractures widths are modelled (See Appendix). The vertical velocity varies in the width of the fractures from 2.5×10^{-5} to 6×10^{-5} m/s for widths between 1–3 cm.

8 Conclusions

- Kimmeridge oil shale is an outcrop in which a fire occurred from 1973–1974 and in 2000, but is presently extinguished.
- The outcrop is sufficiently accessible to do geological observations and taking samples. Moreover the dimensions could be assessed for modelling purposes.
- The formation consists of mudstone with mainly vertical fractures with N–S orientation. In addition there are also some horizontal wedges at bedding interfaces with a dip of five degrees in the NE direction
- The vertical fractures (N–S) had a spacing of 0.25–0.3 m and a fracture width of 0.02 m. The other vertical fractures had the same characteristics. The horizontal wedges had a fracture width of 0.01 m at the exposed front near the coast. These fractures had a spacing of around 0.4 m, but occasionally as large as 0.8 m.

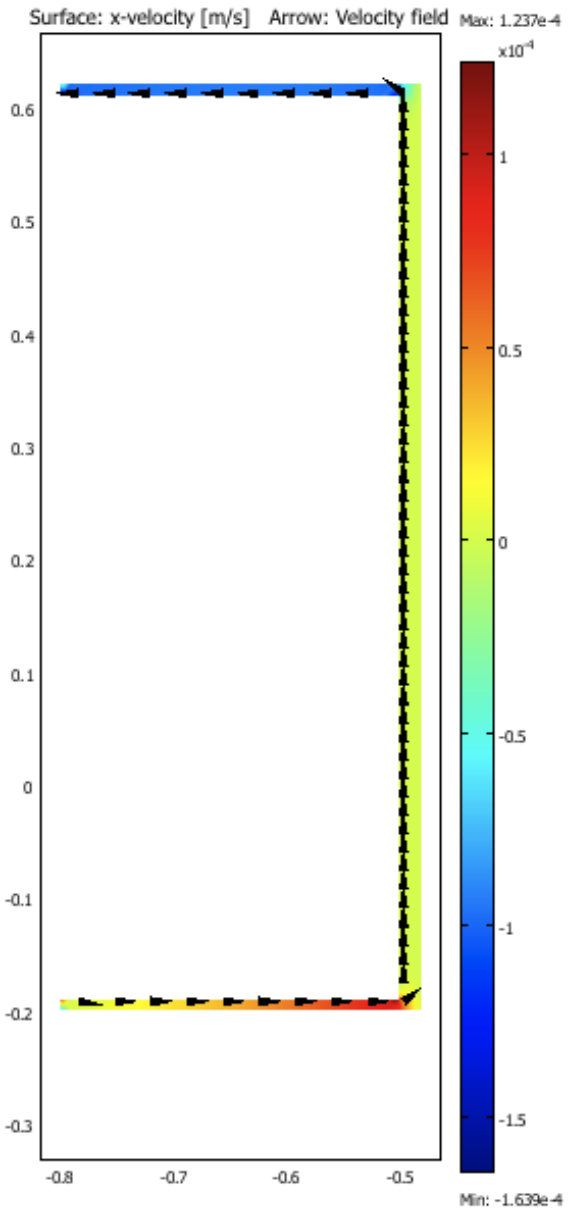

Figure 2: Darcy speed in horizontal direction

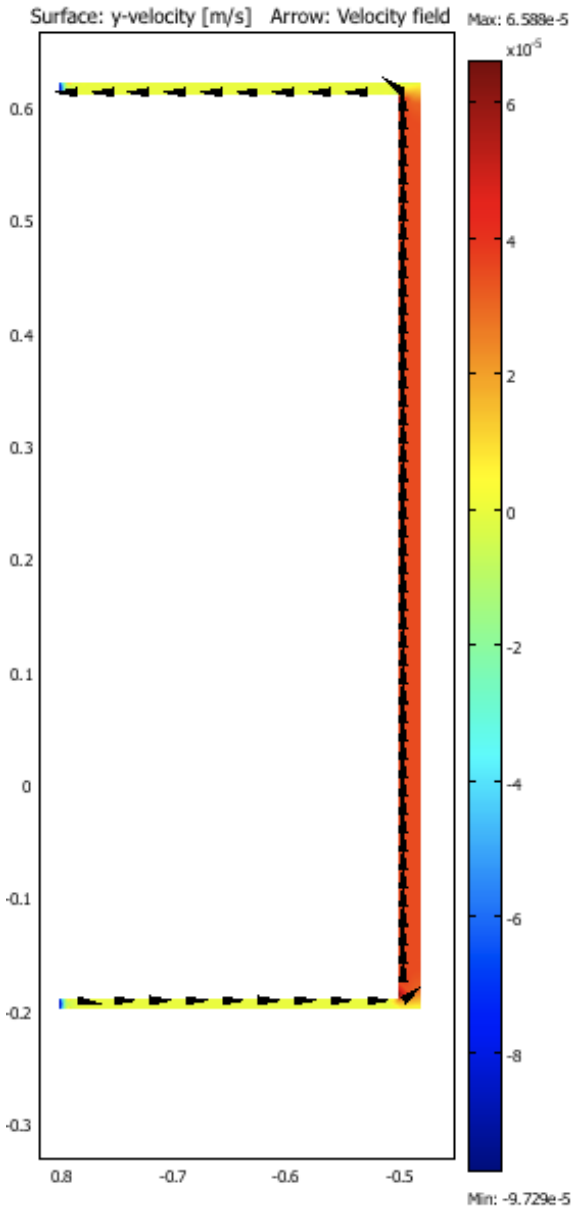

Figure 3: Darcy speed in vertical direction

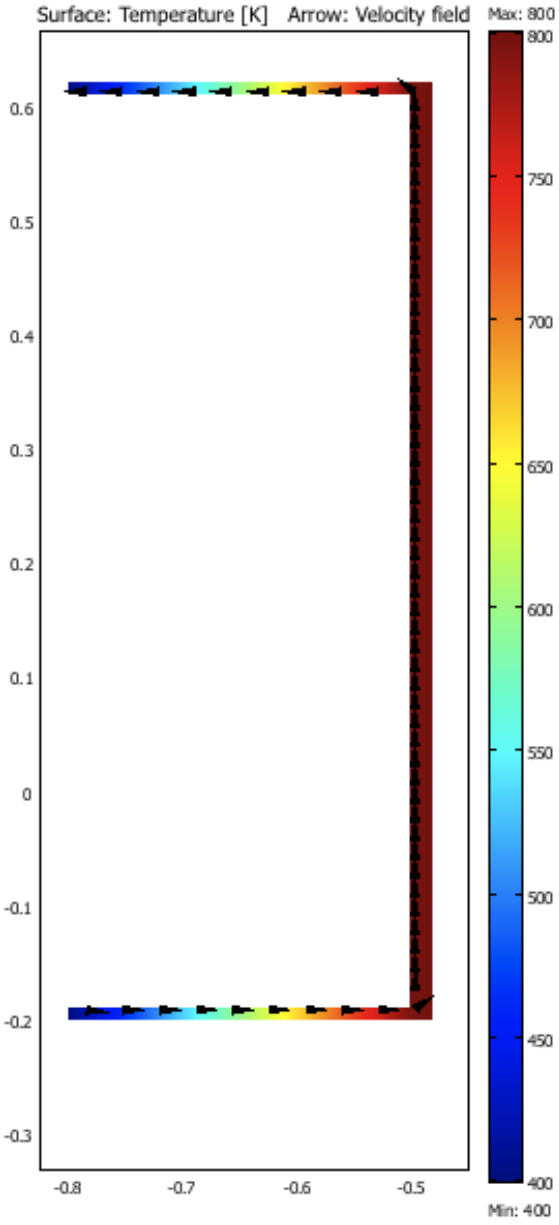

Figure 4: Temperature distribution

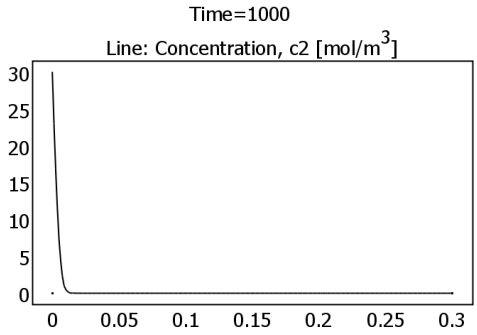

Figure 5: Oxygen diffusion

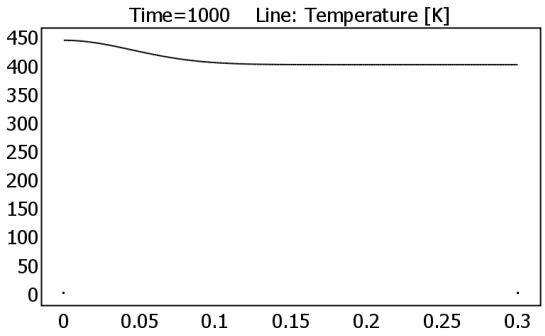

Figure 6: Temperature

- The mineral content of the matrix blocks between the fractures consists of 32 v/v % calcite, 14 % quartz and 21.98 % clay and 0.02 % pyrite with a porosity of 32 % with pores filled with kerogen.
- Ruska permeameter measurements showed a temperature dependent permeability of the matrix blocks between 300 and 600 mD
- Based on the geological assessment a unit cell can be defined bounded from below and above by a horizontal wedge and from the backside by a vertical fracture. The front side is exposed to the air.
- Using an appropriate temperature distribution Stokes equation coupled to a temperature equation has been solved. Flow rates in the fractures were calculated to be between 4–9 m/day. A maximum conversion rate within 1 m from the exposed surface was oil in 48 m^3/day. This corresponds to a burning time of 8 days.
- Reaction rate limited. This is confirmed by a reactive flow calculation
- The temperature field corresponds to the modelling calculations

Acknowledgements

The laboratory experiments were done by Lars van Zelm, as a part of his B.Sc. thesis. Ian West and Steve Etches were excellent guides during the fieldwork, thank you! Arno Mulder helped with the STING and TEMFAST measurements in the field. Karl-Heinz Wolf, Hans Bruining and Rick Donselaar are very enthusiastic, helpful and patient supervisors. Many thanks to you all!

References

[1] W. J. Arkell, C. W. Wright, and H. J. Osborne White. *The Geology of the Country around Weymouth, Swanage, Corfe and Lulworth*. HM Stationery Off., 1947 (reprinted 1953).

[2] D.I. Cole. Observations on a burning cliff. *Proceedings of the Dorset Natural History and Archaeological Society*, 96:16–19, 1975.

[3] B. M. Cox and R. W. Gallois. The stratigraphy of the dorset type area and its correlation with some other kimmeridgian sequences. *Institute of Geological Sciences*, 80 (4):1–44, 1981.

[4] E. J. Ebukanson and R. R. F. Kinghorn. Jurassic mudrock formations of southern england: Lithology, sedimentation rates and organic carbon content. *Journal of Petroleum Geology*, 13(2):221–288, 1990. doi: 10.1111/j.1747-5457.1990.tb00841.x. URL http://dx.doi.org/10.1111/j.1747-5457.1990.tb00841.x.

[5] X. M. Jiang, X. X. Han, and Z. G. Cui. New tecnology for the comprehensive utilization of chinese oil shale resources. *Elsevier, ScienceDirect*, 413A, 2006.

[6] J. H. S. Macquaker and R. L. Gawthorpe. Shale oil; the elusive energy. *Journal of Sedimentary Petrology*, 63(6):1129–1143, 1993.

[7] S. J. Pearson, J. E. A. Marshall, and A. E. S. Kemp. The White Stone Band of the Kimmeridge Clay Formation, an integrated high resolution approach to understanding environmental change. *Journal of Georlogical Society*, 161:675–683, 2004.

ISSN 0016-7649. URL http://eprints.soton.ac.uk/7809.

[8] E. V. Sokol, I. S. Novikov, Ye. Vapnik, and V. V. Sharygin. Gas fire from mud volcanoes as a trigger for the appearance of high-temperature pyrometamorphic rocks of the hatrurim formation (dead sea area). *Institute of Geological Sciences*, 413A(3):474–480, April 2007. doi: 10.1134/S1028334X07030348. URL http://www.springerlink.com/content/bl0404609xk01108/.

[9] Graham P. Weedon, Hugh C. Jenkyns, Angela L. Coe, and Stephen P. Hesselbo. Astronomical calibration of the jurassic time-scale from cyclostratigraphy in british mudrock formations. *Philosophical Transactions of the Royal Society of London*, 357(1757):1787–1813, July 1999. doi: 10.1098/rsta.1999.0401. URL http://rsta.royalsocietypublishing.org/content/357/1757/1787.abstract.

[10] Ian West. Geology of the wessex coast, November, January 2007,2008. URL http://www.soton.ac.uk/~imw/kim.htm.

[11] Ian West. Kimmeridge- the blackstone-oil shale, October 2008. URL http://www.soton.ac.uk/~imw/kimblack.htm.

[12] Ian West. Burning cliffs of dorset-oil shale fires, November, January 2007–2008. URL http://www.soton.ac.uk/~imw/kimfire.htm.

[13] Karl-Heinz Wolf. *The interaction between coal fires and their roof rocks*. PhD thesis, Delft University of Technology, Delft, the Netherlands, 2006.

[14] Karl-Heinz Wolf and J. Bruining. Modelling the interaction between underground coal fires and their roof rocks. *Fuel*, 86(17–18):2761–2777, March 2007. doi: 10.1016/j.fuel.2007.03.009. URL http://www.sciencedirect.com/science/article/B6V3B-4NDDNKF-4/2/301e463153f26332afa87ebbfabe36ac.

[15] Walter L. Youngquist. Shale oil; the elusive energy. *Hubbert Center Newsletter*, 98(4), 1998. URL http://hubbert.mines.edu/news/Youngquist_98-4.pdf.

[16] Lars Zelm van. B.sc. thesis. B.Sc. thesis, 2008.

Appendices

A Deriving the dimensionless forms

The stream equation

$$\frac{\partial}{\partial X}\frac{\partial \psi}{\partial X} + \frac{\partial}{\partial Z}\frac{\partial \psi}{\partial Z} = -\frac{\kappa}{\mu}\rho g \beta \frac{\partial T}{\partial X}$$

We define the parameters X, Z, T and ψ

$$X = X_D L \qquad Z = Z_D L$$
$$\psi = \psi_D \psi_R \qquad T = T_D T_R$$

Substitution of these parameters into equation (9)

$$\frac{\partial}{\partial X_D L}\frac{\partial \psi_D \psi_R}{\partial X_D L} + \frac{\partial}{\partial Z_D L}\frac{\partial \psi_D \psi_R}{\partial Z_D L} = -\frac{\kappa}{\mu}\rho g \beta \frac{T_R}{L}\frac{\partial T_D}{\partial X_D}$$

$$\frac{\partial^2 \psi_D}{\partial X_D^2} + \frac{\partial^2 \psi_D}{\partial Z_D^2} = -\frac{\kappa}{\mu}\rho g \beta T_R \frac{L}{\psi_R}\frac{\partial T_D}{\partial X_D}$$

Where - $\frac{\kappa}{\mu}\rho g \beta T_R \frac{L}{\psi_R} = Gr$

The heat equation

$$-\left(\frac{\partial \psi}{\partial Z}\frac{\partial T}{\partial X}\right) + \left(\frac{\partial \psi}{\partial X}\frac{\partial T}{\partial Z}\right) = \chi\left(\frac{\partial^2 T}{\partial X^2} + \frac{\partial^2 T}{\partial Z^2}\right)$$

Substituting the defined parameters into equation (10)

$$\frac{\psi_R T_R}{L^2}\left(\left(\frac{\partial \psi_D}{\partial X_D}\frac{\partial T_D}{\partial Z_D}\right) - \left(\frac{\partial \psi_D}{\partial Z_D}\frac{\partial T_D}{\partial X_D}\right)\right) = \frac{T_R}{L^2}\chi\left(\frac{\partial^2 T_D}{\partial X_D^2} + \frac{\partial^2 T_D}{\partial Z_D^2}\right)$$

$$\left(\frac{\partial \psi_D}{\partial X_D}\frac{\partial T_D}{\partial Z_D}\right) - \left(\frac{\partial \psi_D}{\partial Z_D}\frac{\partial T_D}{\partial X_D}\right) = \frac{\chi}{\psi_R}\left(\frac{\partial^2 T_D}{\partial X_D^2} + \frac{\partial^2 T_D}{\partial Z_D^2}\right)$$

Where $\frac{\psi_R}{\chi} = Pr$

B Geology

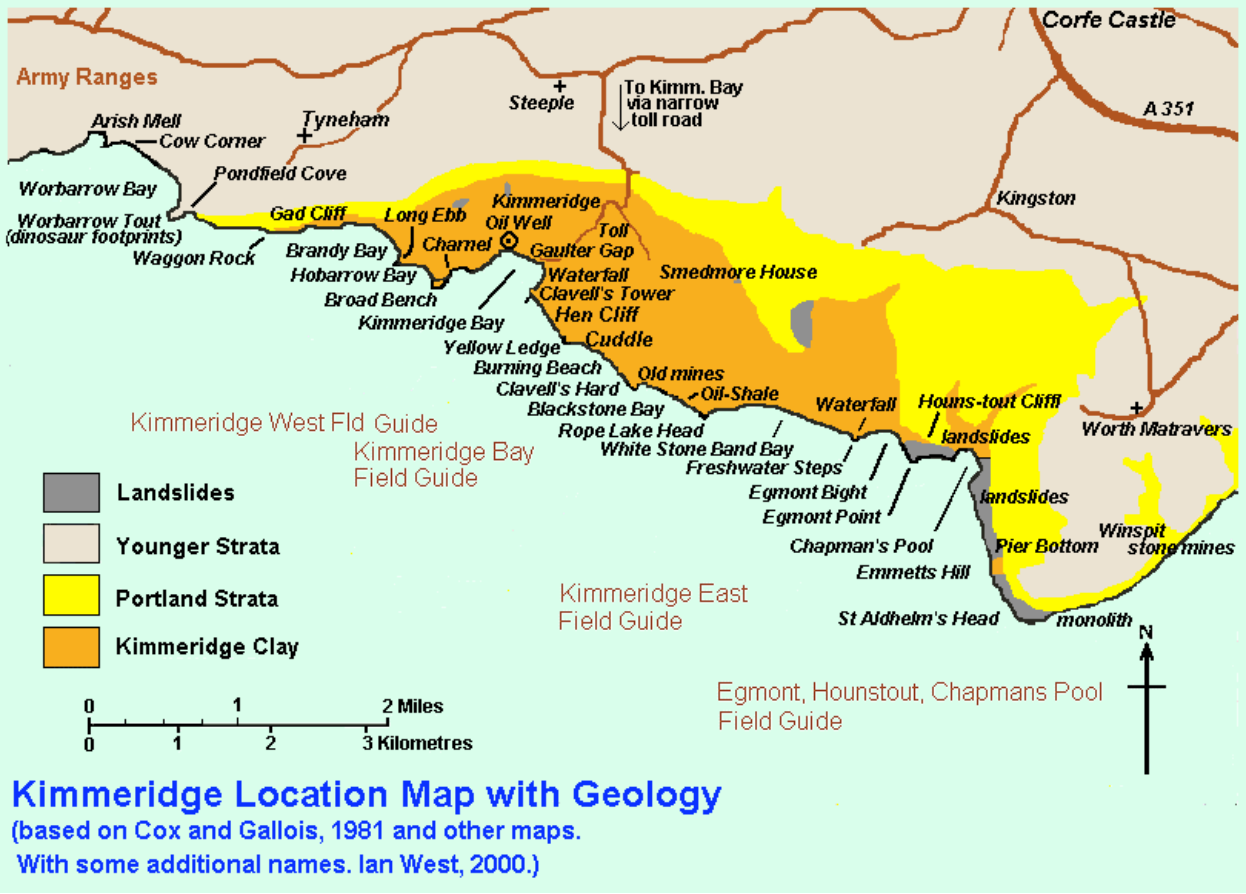

Figure 7: Location of Kimmeridge Bay in Dorset, South England

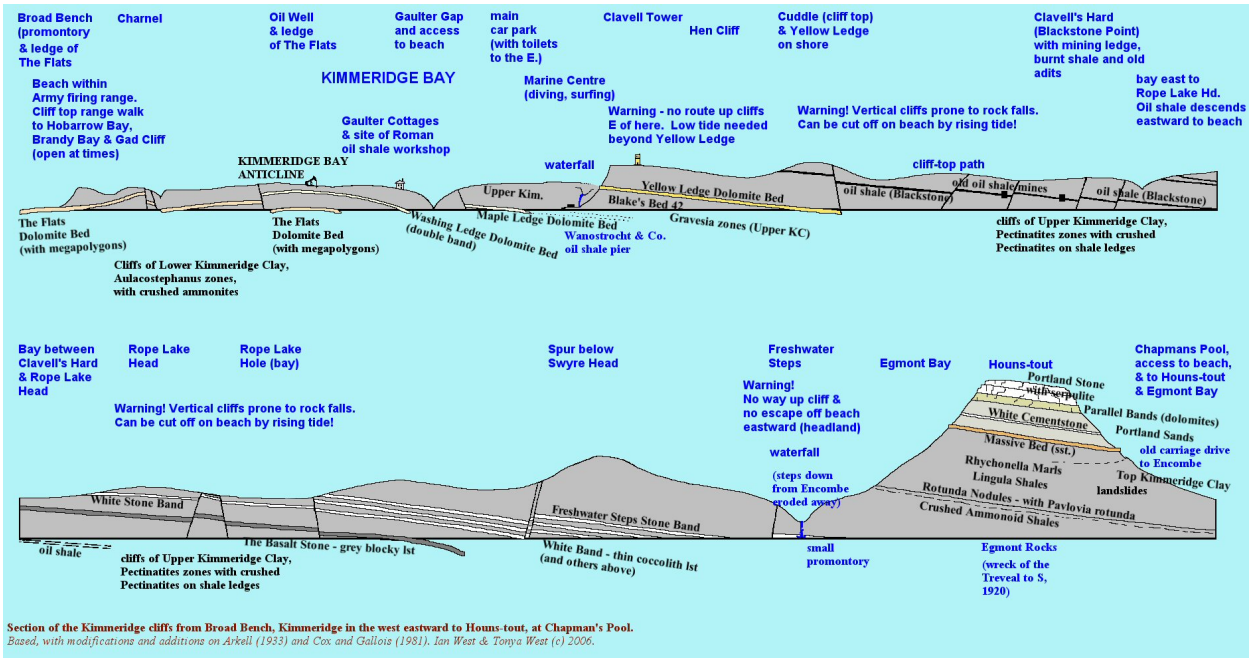

Section of the Kimmeridge cliffs from Broad Bench, Kimmeridge in the west eastward to Houns-tout, at Chapman's Pool.
Based, with modifications and additions on Arkell (1933) and Cox and Gallois (1981). Ian West & Tonya West (c) 2006.

Figure 8: Geological cross section of the Kimmeridge Clay Formation

C Field observations, measurements and interpretations

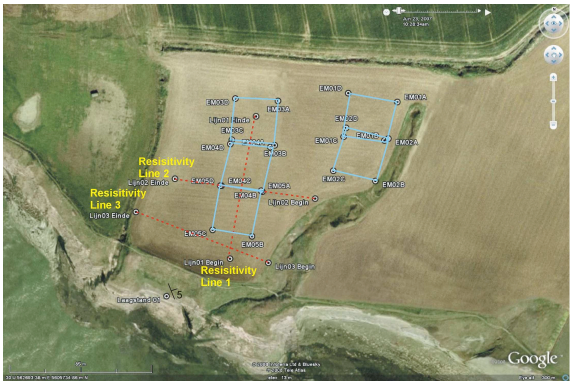

Figure 9: Locations where the TemFast en STING measurements were done

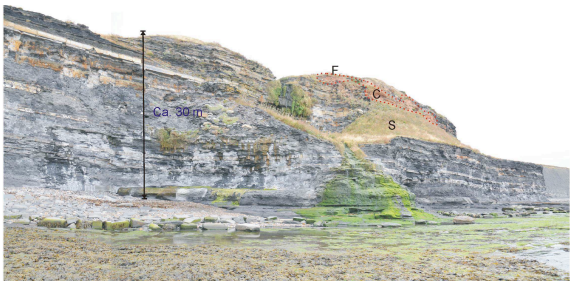

Figure 10: BurntCliffKimmeridge

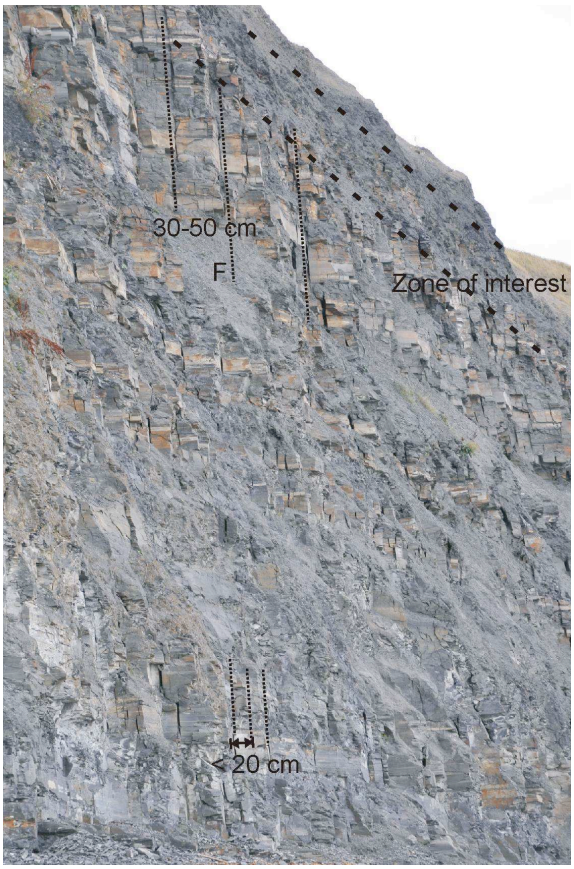

Figure 11: Spacing of the faults

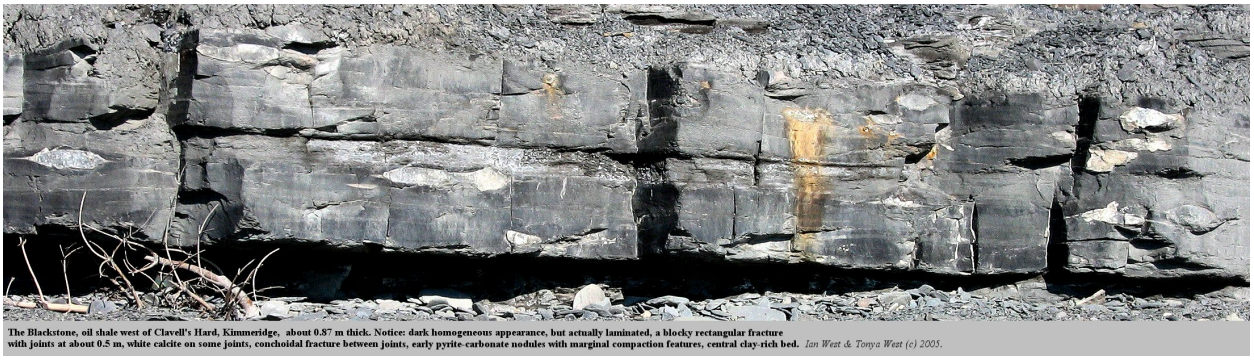

Figure 12: Close up of the Blackstone, wedges en vertical fratures clearly visible

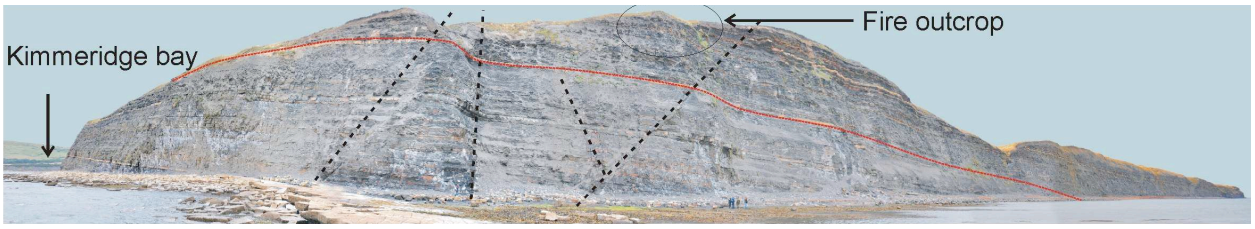

Figure 13: Panorama view of the Kimmeridge Clay formation

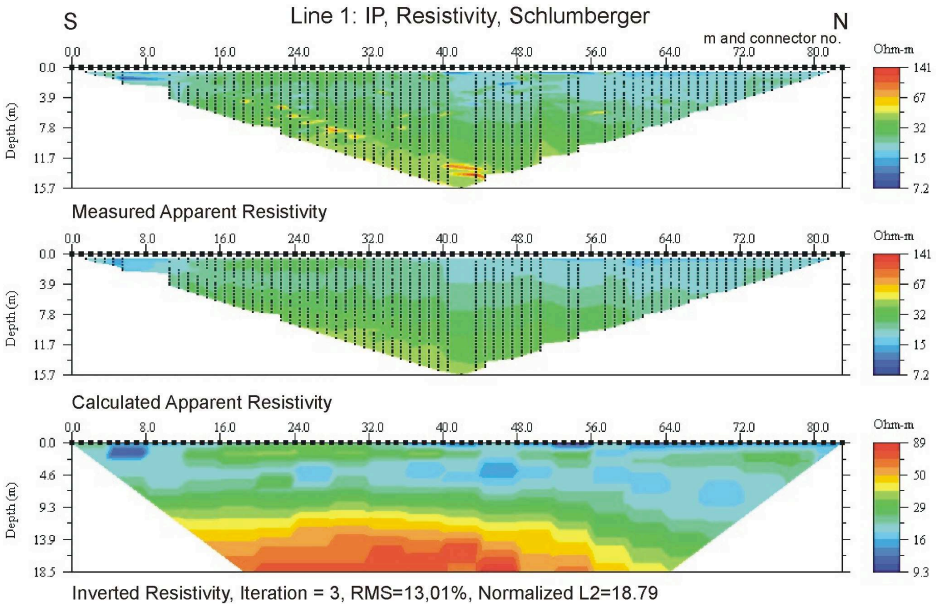

Figure 14: Result Sting Line 1 Schlum

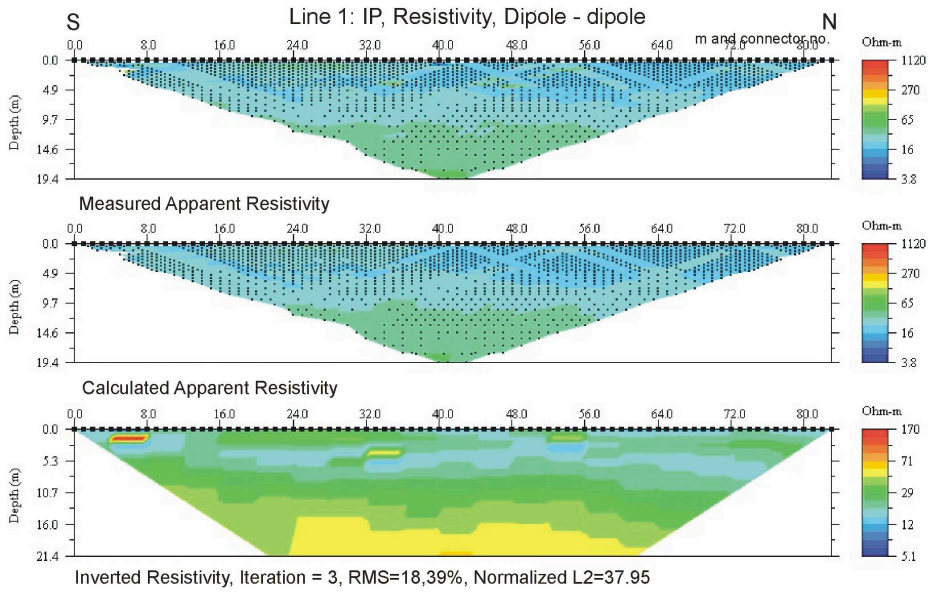

Figure 15: Result Sting Line 1 Dipole

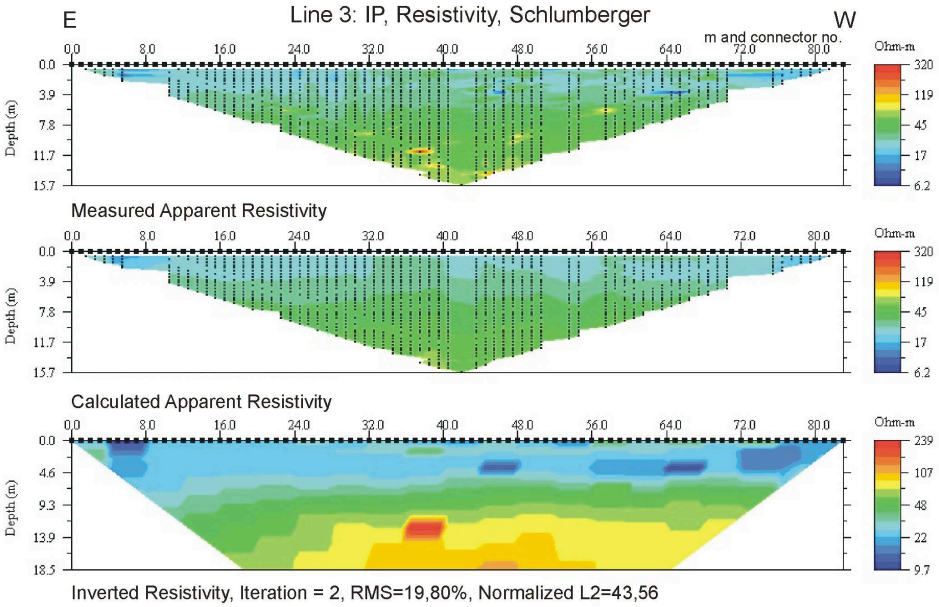

Figure 16: Result Sting Line 3 Schlum

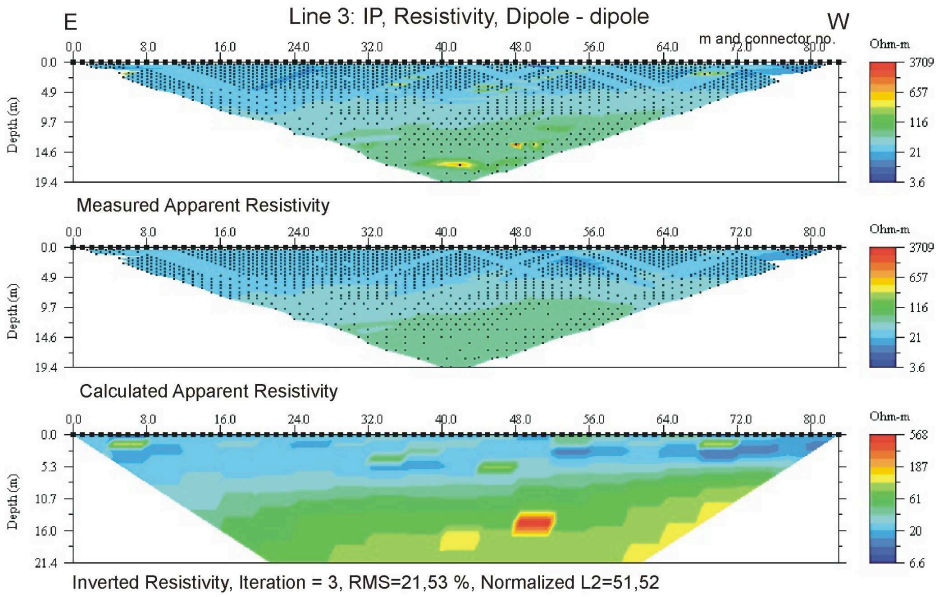

Figure 17: Result Sting Line 3 Dipole

D Lab experiments

D.1 Methodology

D.1.1 Permeability and porosity measurements

Figure 18: Side view from a core sample baked at 900 °C

In order to do the experimental measurements on porosity and permeability core samples were prepared with a height of 3 cm and a diameter of 2.5 cm. Although the samples were prepared with utmost care, the brittle behaviour of the oil shale made it difficult to get perfect core samples. The 9 best samples of a total of 15, were used to perform the measurements on. Nevertheless, some of the samples were glued together to minimise the influence of the fractures on the samples. For the dry porosity measurement the Ultrapycnometer was used to measure the matrix volume and the true density of the samples. The instrument makes use of the next formula.

$$(V - V_{ma})P_1 = (V - V_{ma} + \Delta V)P_2$$

, where V is the volume of the sample holder m^3, V_{ma} is the matrix volume of the sample m^3 and Δ V is the volume change m^3. This formula implies a thermal equilibrium. Caution should be taken with the placing and removing of samples holder to not to disturb this equilibrium. In the formula, the unknown and needed parameter is the matrix volume V_{ma}. By changing the pressure P over the cell in which the core is placed, a change in volume is obtained (V). This volume change is obtained by saturating the core with air, resulting in a volume of the connected pores. For this

experiment, helium is used as a displacing gas to obtain a reliable result of the effective porosity. Subtracting the volume change from the sample holder volume V, the needed V_{ma} is obtained. From this the effective porosity can be calculated by a simple formula.

$$\phi = \frac{(V_b - V_{ma})}{V_b}$$

, where V_b is the bulk volume m^3. To acquire a significant amount of data to assess the quality of the measurements, multiple runs were performed. Each core was tested 5 times, resulting in a large amount of porosity data. The outliers were deleted, especially those that influenced the average value too much (higher than 10 % and below 1 %).

The second part of this experiment was to measure the dry permeability of the core samples. This was done with the Ruska gas permeameter which measures the vertical flow through the samples over a specific pressure-drop. The temperature can be read from the apparatus, which determines the viscosity of the specific gas used (N_2). All these parameters are used in Darcy's law, which allows the dry gas permeability of the sample to be calculated.

$$\kappa = \frac{\mu Q L}{A P}$$

, where A is the contact area m^2, Q the flow-rate m^3/per/second and L is the length/height m. Each core was tested 3 times at least to ensure a good reliable result of the measurement. After the complete run, the permeability values were sorted by deleting values higher than 100 mD and lower than 2 mD.

Both experiments will be repeated after the samples have been heated at certain specific temperatures.

D.1.2 XRF / XRD Analysis

To determine the mineral composition of the oil shale X-ray fluorescence (XRF) and X-ray diffraction (XRD) have been used in addition to a thin section analysis. Both methods provide a qualitative and quantitative measurement of the elements and minerals present. The first method uses X-rays to move atoms from one shell to another, thereby admitting an element specific energy. This energy is measured and can be used for determination and concentration. So it provides both a qualitative and quantitative measurement of the elements and minerals present. The determination process used by X-ray diffraction is based on the arrangement of the atoms, which are bond in a specific crystalline structure. The reflections of X-rays on the different planes of the crystal are specific and give each mineral its own diffraction pattern. The result is a graph with different peaks with different magnitude representing the different angles of diffraction, the so-called 2-theta-scale, and its relative presence in the sample. Two samples were used, one in-situ sample and one heated at 1000 °C for one hour. Before the experiments, the samples were crushed to homogenize the material and thereby obtaining the best results.

The tests were done by Ron Penners in the Geotechnology laboratories (XRF) and by Ruud Hendrixk of X-Ray Facilities of the Department of Materials Science and Engineering at the TU Delft (XRF and XRD).

D.1.3 Thin Section Analysis

Apart from the XRF / XRD analysis, the mineral composition can also be studied by analysing thin sections of the rock. Moreover, the amount of organic material can be estimated and compared to results from the porosity and permeability measurements. Two thin sections were prepared, one of a kerogen-saturated sample and one of a sample partially saturated with kerogen. These thin sections were photographed using a microscopic camera, which allows for accurate determination. Two photographs were examined and some minerals were detected that were also shown in the XRD and XRF analysis. One of the photographs is taken with normal light and the other is taken with specific polarised light.

D.2 Results

Table 5: Dry Permeability in situ

No.	Area (cm3)	Length (cm)	Pres. (atm)	Visc. (cp)	Flowrate (cm^3/s)	Permeability (mD)	Side
C	4.95	3.06	1.00	0.01747	61.00	653.88	up-down
C	4.91	3.05	0.50	0.01747	54.00	1157.69	up-down
C	4.91	3.06	0.50	0.01747	50.00	1071.94	sideways
	4.92						
A	4.91	2.99	0.25	0.01747	16.00	672.14	up-down
A	4.91	3.00	0.50	0.01747	32.00	674.38	up-down
A	4.91	2.99	0.50	0.01747	26.00	546.11	sideways
	4.91						
E	5.07	3.02	0.50	0.01747	2.30	47.74	sideways
E	4.99	3.01	1.00	0.01747	3.00	31.13	sideways
E	4.95	3.03	0.25	0.01747	1.50	62.26	up-down
	5.00						
L	4.75	3.08	0.50	0.01747	4.20	92.07	sideways
L	4.81	3.07	1.00	0.01747	7.00	76.73	sideways
L	4.91	3.08	0.25	0.01747	6.00	263.07	up-down
	4.82						
J	4.99	3.05	0.50	0.01747	0.52	11.11	up - down
J	4.79	3.05	0.50	0.01748	0.70	14.97	sideways
J	4.99	3.05	1.00	0.01747	0.45	4.81	sideways
	4.92						
G	4.87	3.03	0.25	0.01753	8.60	370.32	up-down
G	4.83	3.04	0.50	0.01743	11.50	247.00	sideways
G	4.91	3.03	0.50	0.01743	12.00	256.89	sideways
	4.87						
M	4.95	3.08	0.25	0.01747	10.00	430.42	sideways
M	4.99	3.07	0.50	0.01747	15.00	321.77	sideways
M	4.87	3.08	0.50	0.01747	15.00	322.82	up-down
	4.94						
H	4.95	3.04	0.25	0.01747	26.00	1122.37	up-down
H	4.79	3.05	0.50	0.01747	36.00	779.58	up-down
H	4.83	3.04	0.25	0.01747	27.00	1165.54	sideways
	4.86						
I	4.87	3.05	0.50	0.01747	9.60	205.68	sideways
I	4.95	3.03	1.00	0.01747	16.00	170.28	sideways
I	4.91	3.03	0.25	0.01747	8.00	340.56	up-down
	4.91						

Table 6: Dry Permeability at different temperatures

No.	Temp	Pres. (atm)	Visc. (cp)	Flowrate (cm3 / s)	Permeability (mD)	Permeability (mD)
C	600	0,25	0,017	45	1930,59	
C		0,25	0,017	47	2016,39	
C		0,25	0,017	38	1630,27	
A	900	0,25	0,017	7,2	302,63	
A		0,5	0,017	14	295,212	590,424
A		1	0,017	26	273,212	463,904
E		0,25	0,017	2,5	103,83	
E		0,5	0,017	3,4	70,6074	
E		1	0,017	4,7	48,8022	
L	900	0,25	0,017	5,4	236,899	293,930
L		0,5	0,017	11	241,286	285,156
L		1	0,017	20	219,351	
J	600	0,25	0,017	30	1282,7	534,476
J		0,5	0,017	40	855,2	384,82
J		1	0,017	52,5	561,200	267,238
G	300	0,25	0,017	2,4	102,99	163,161
G		0,5	0,017	4,25	91,4903	84,0039
G		1	0,017	4,8	51,495	55,9257
			0,017			
M	1000	0,25	0,017	11,6	499,288	
M		0,5	0,017	32	686,437	
M		0,5	0,017	26	559,574	
H	1000	0,25	0,017	20	863,364	
H		0,5	0,017	38	822,894	
H		0,5	0,017	39	841,780	
I	300	0,25	0,017	12	514,212	
I		0,5	0,017	24	510,84	
I		1	0,017	77	819,473	
		0,5	0,017	37	792,744	
		0,5	0,017	36	766,26	
		1	0,017	59	627,908	

Table 7: Dry Porosity In Situ

No.	Diam.	Height	Vol.	Weight	Por. (1)	Por. (2)	Por. (3)	Por. (4)	Por. (5)
C	2.51	3.06	15.14	27.09	6.36	5.28	6.26	2.55	5.20
C	2.50	3.05	14.97						
C	2.50	3.06	15.02						
			15.04						
A	2.50	2.99	14.68	26.65	4.77	1.89	3.47	3.86	1.72
A	2.50	3.00	14.73						
A	2.50	2.99	14.68						
			14.69						
E	2.54	3.02	15.30	27.12	1.65	4.20	6.03	0.92	8.72
E	2.52	3.01	15.01						
E	2.51	3.03	14.99						
			15.10						
L	2.46	3.08	14.63	27.40	5.07	0.28	1.70	0.74	1.70
L	2.48	3.07	14.76						
L	2.50	3.08	15.11						
			14.83						
J	2.52	3.05	15.21	26.78	8.67	11.49	10.01	6.32	5.57
J	2.47	3.05	14.61						
J	2.52	3.05	15.21						
			15.01						
G	2.49	3.03	14.75	27.32	1.58	7.12	-0.38	1.43	2.05
G	2.48	3.04	14.68						
G	2.50	3.03	14.87						
			14.77						
M	2.51	3.08	15.24	27.51	4.45	7.01	4.45	2.42	3.44
M	2.52	3.07	15.31						
M	2.49	3.08	15.00						
			15.18						
H	2.51	3.04	15.04	26.48	7.02	10.11	4.32	4.96	7.32
H	2.47	3.05	14.61						
H	2.48	3.04	14.68						
			14.78						
I	2.49	3.05	14.85	26.69	10.15	10.06	6.37	5.47	7.43
I	2.51	3.03	14.99						
I	2.50	3.03	14.87						
			14.91						

Table 8: Dry Porosity at different temperatures

Weight	No.	Temp	Diam.	Height	Vol.	Por(1)	Por(2)	Por(3)	Por(4)	Por(5)
20,98	C	600	2,45	3,05	14,379	48,7	46,695	48,188	46,589	46,553
	C		2,48	3,05	14,73					
	C		2,53	3,05	15,333					
					14,81					
15,51	A	900	2,47	2,97	14,231	64,560	63,199	62,933	62,789	62,706
	A		2,47	2,95	14,135					
	A		2,45	2,98	14,049					
					14,14					
	E	not	2,54	3,02	15,303	9,546	9,0927	9,047	8,9888	8,9808
	E		2,52	3,01	15,013					
	E		2,51	3,03	14,993					
16	L	900	2,42	3,03	13,937	64,366	63,135	62,953	62,832	62,79
	L		2,46	3,04	14,449					
	L		2,47	3,03	14,519					
					14,301					
21,26	J	600	2,45	3,04	14,332	47,222	45,162	45,025	44,940	44,962
	J		2,48	3,03	14,636					
	J		2,49	3,05	14,852					
					14,607					
26,5	G	300	2,45	3,03	14,284	4,7816	2,9083	2,2970		
	G		2,5	3,03	14,873	10,266	9,8962	9,8243	9,7857	9,7647
	G		2,51	3,05	15,092					
					14,750					
16,07	M	1000	2,49	3,05	14,852	65,469	64,139	63,995	63,89	63,845
	M		2,5	3,07	15,070					
	M		2,48	3,05	14,73					
					14,89					
15,41	H	1000	2,48	3,03	14,636	66,76	65,540	65,370	65,260	65,228
	H		2,47	3,03	14,519					
	H		2,47	3,01	14,423					
					14,526					
25,81	I	300	2,43	3,03	14,052	7,3900	9,2269	8,273	6,6801	5,4730
	I		2,49	3,04	14,803	11,420	11,502	11,455	11,410	11,387
	I		2,48	3,02	14,588					
					14,481					

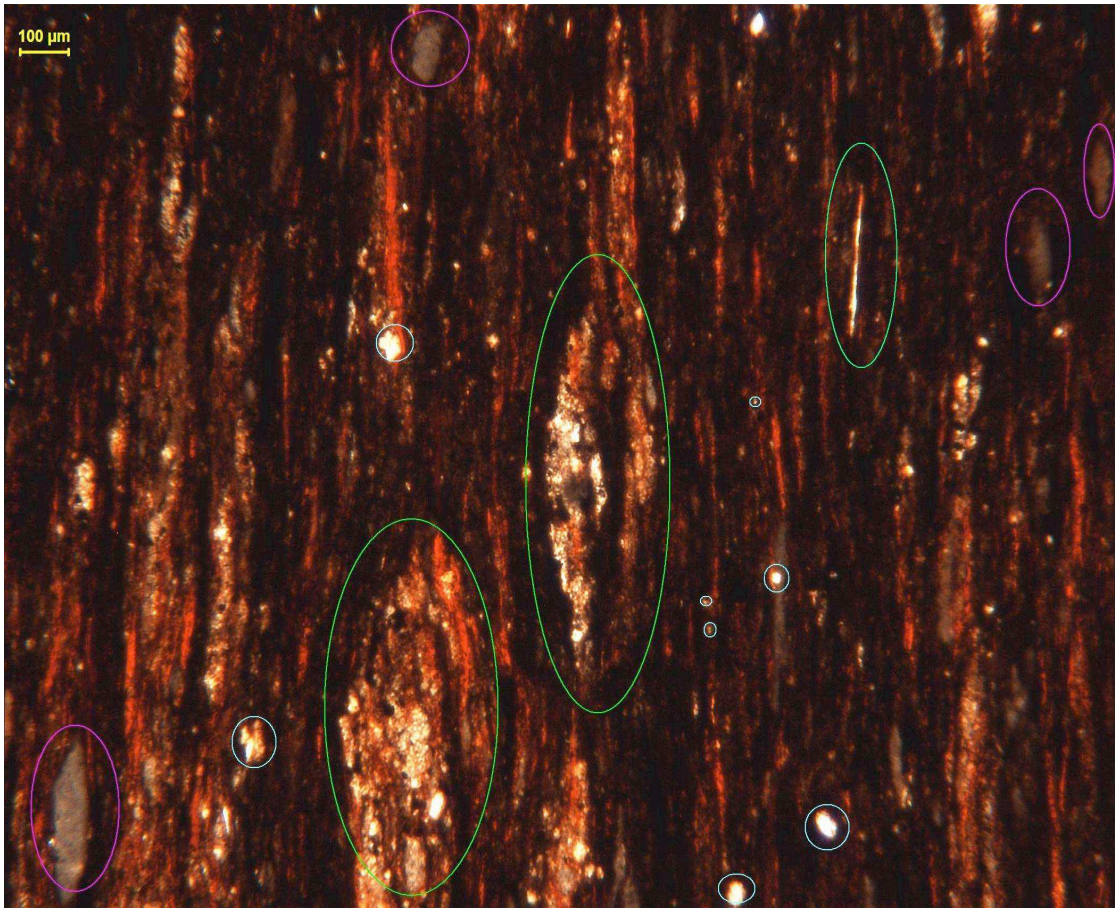

Figure 19: Thin section I (vertical)

Table 9: Thin section I

Colour	Mineral	Volume % (estimated)	Remark
Green circle	Calcite/Calcium carbonate	35	Little fragments make up mineral, lights up bright, but can extinguish in polarised light
Light blue circle	Quartz	10	Small bright modules of quartz, do not extinguishin polarised light
Pink circle	Kaolinite/Montmorillo	10	Vague colour in polarised light. Abundant
Red/brown	Organic matter	45	Organic material present in abundance

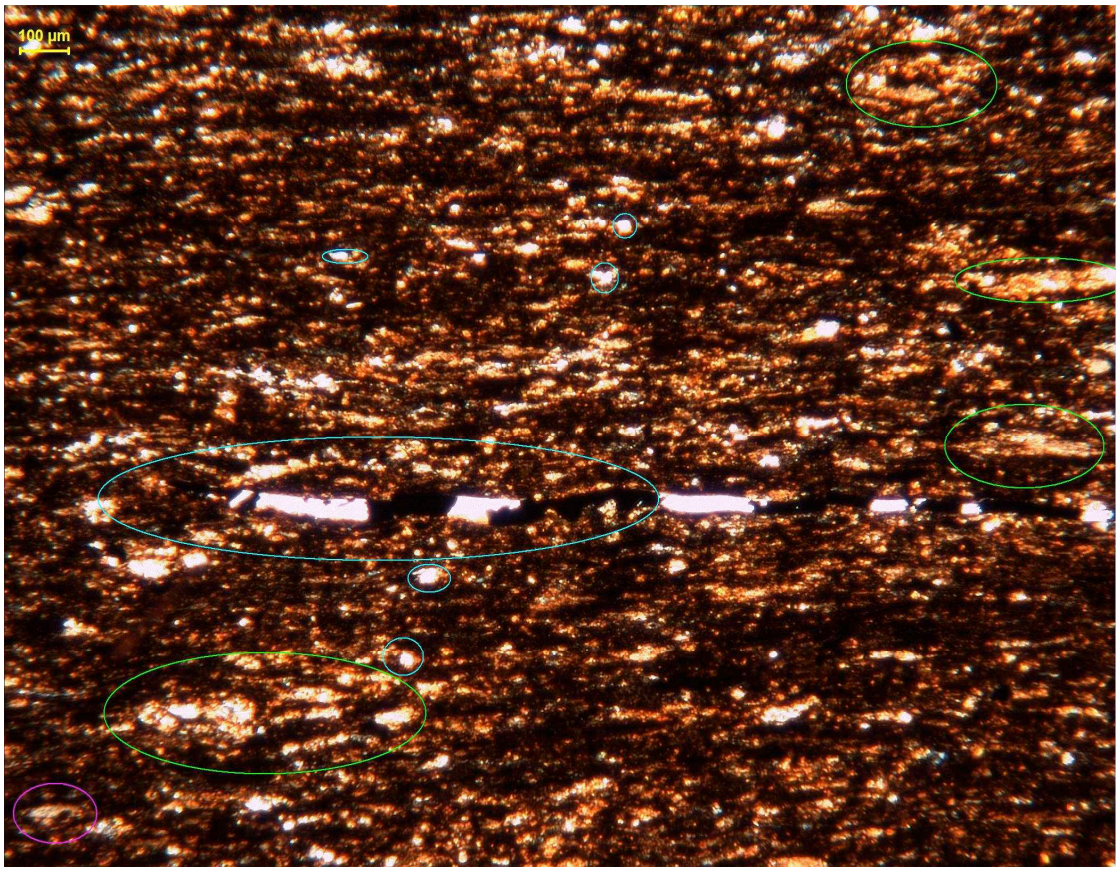

Figure 20: Thin section II (horizontal)

Table 10: Thin section II

Colour	Mineral	Volume % (estimated)	Remark
Green circle	Calcite/Calcium carbonate	45	
Light blue circle	Quartz	20	Perfect sample of large quartz vein. Small bright modules
Pink circle	Kaolinite/Montmorillo	5	Vague colour in polarised light. Abundant
Red/brown	Organic matter	30	Organic material present in abundance

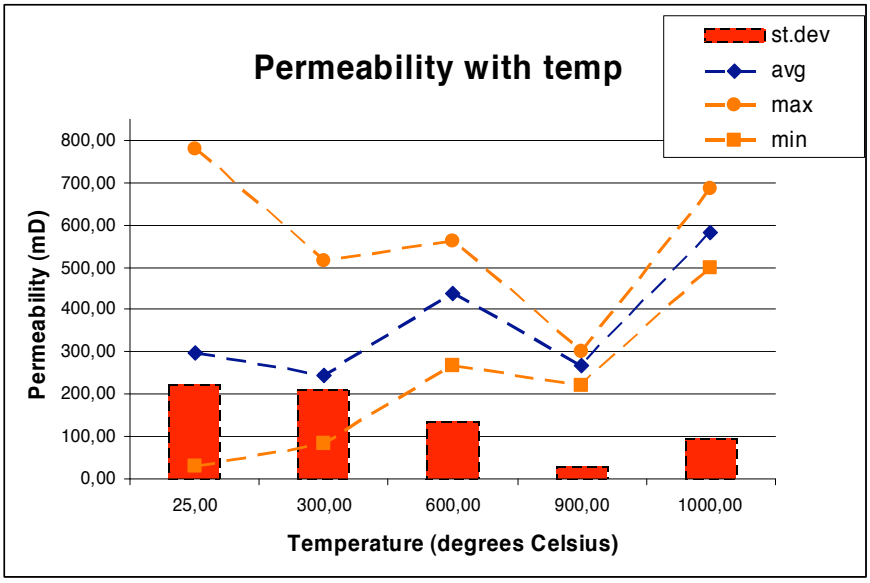

Figure 21: Perm vs Temp

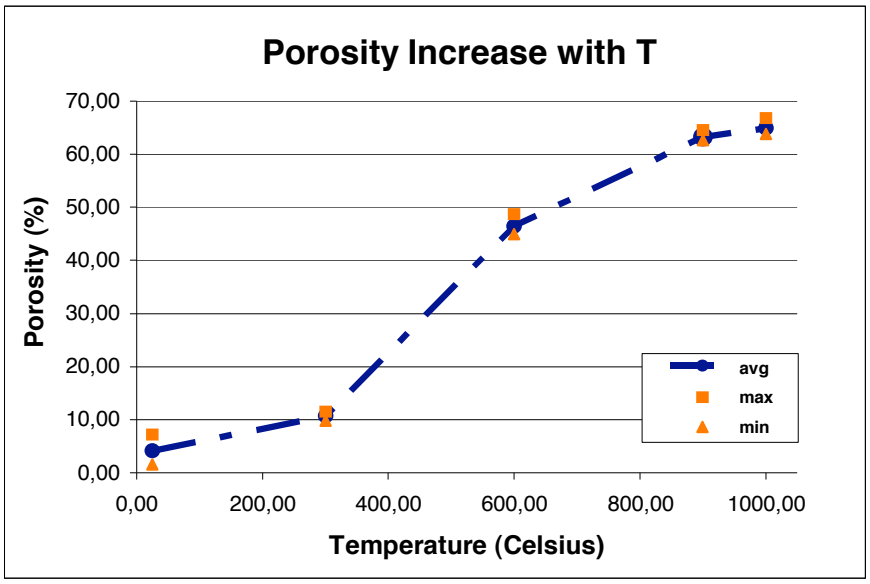

Figure 22: Por vs Temp

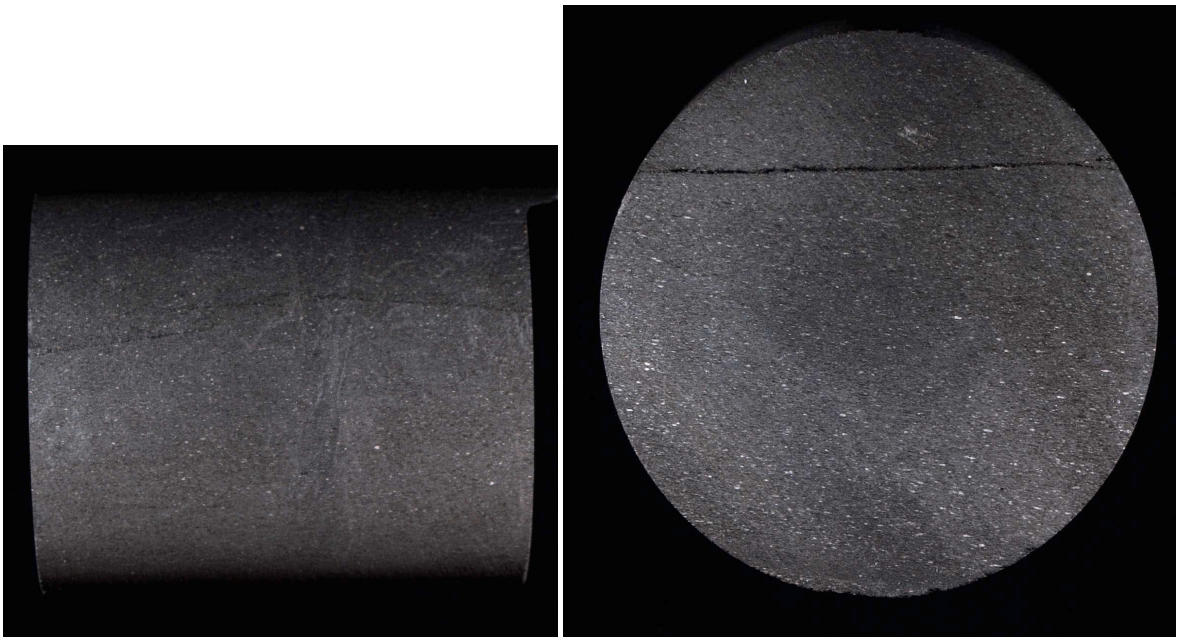

(a) Side View (b) Top View

Figure 23: Natural sample of C

E Modelling results

Four scenarios with variable widths are modelled. The plots indicate the vertical velocity of fractures with a width of 1 cm, 1.5 cm, 2.5 cm, 3 cm, respectively.

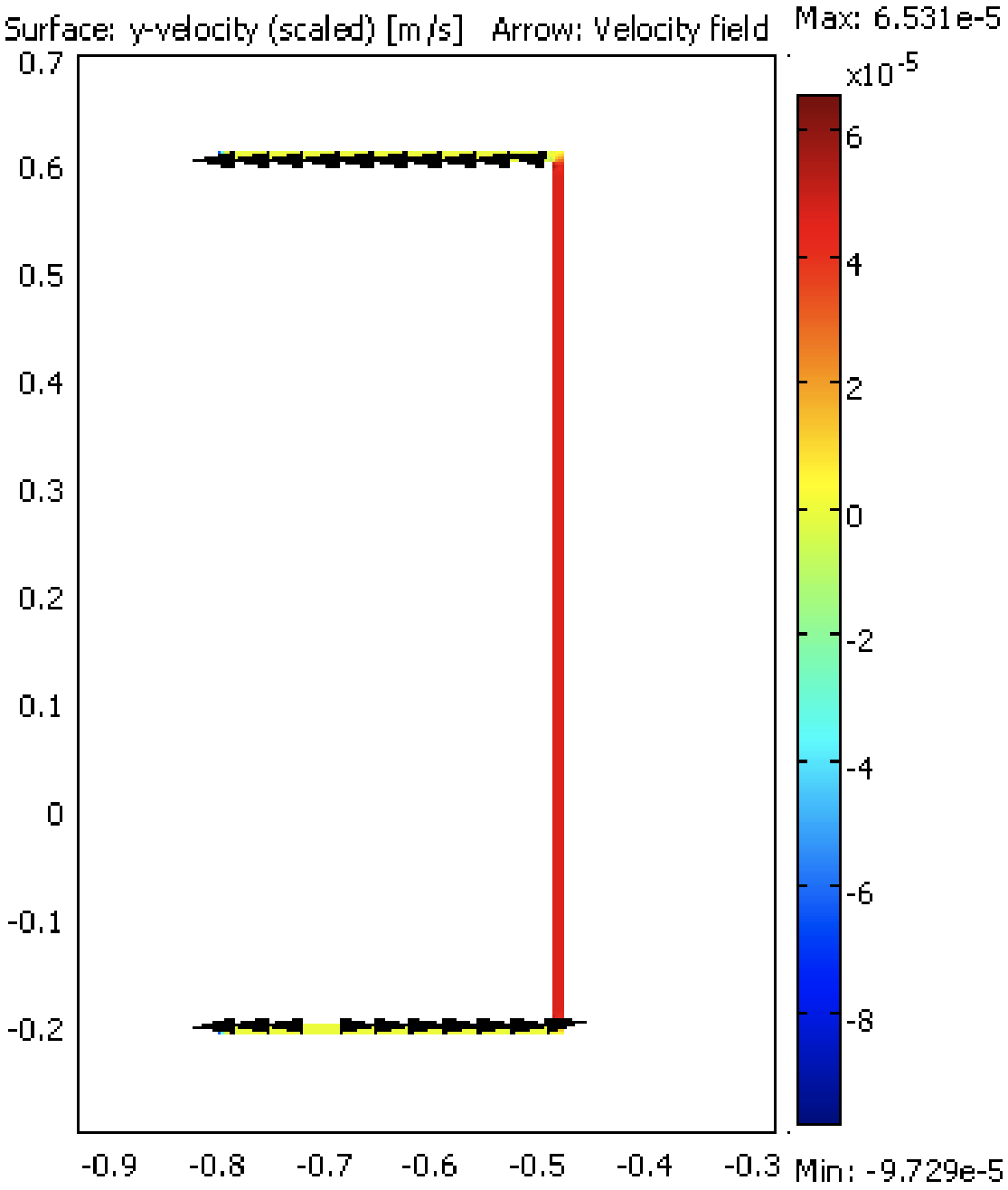

Figure 24: Frac 1 cm

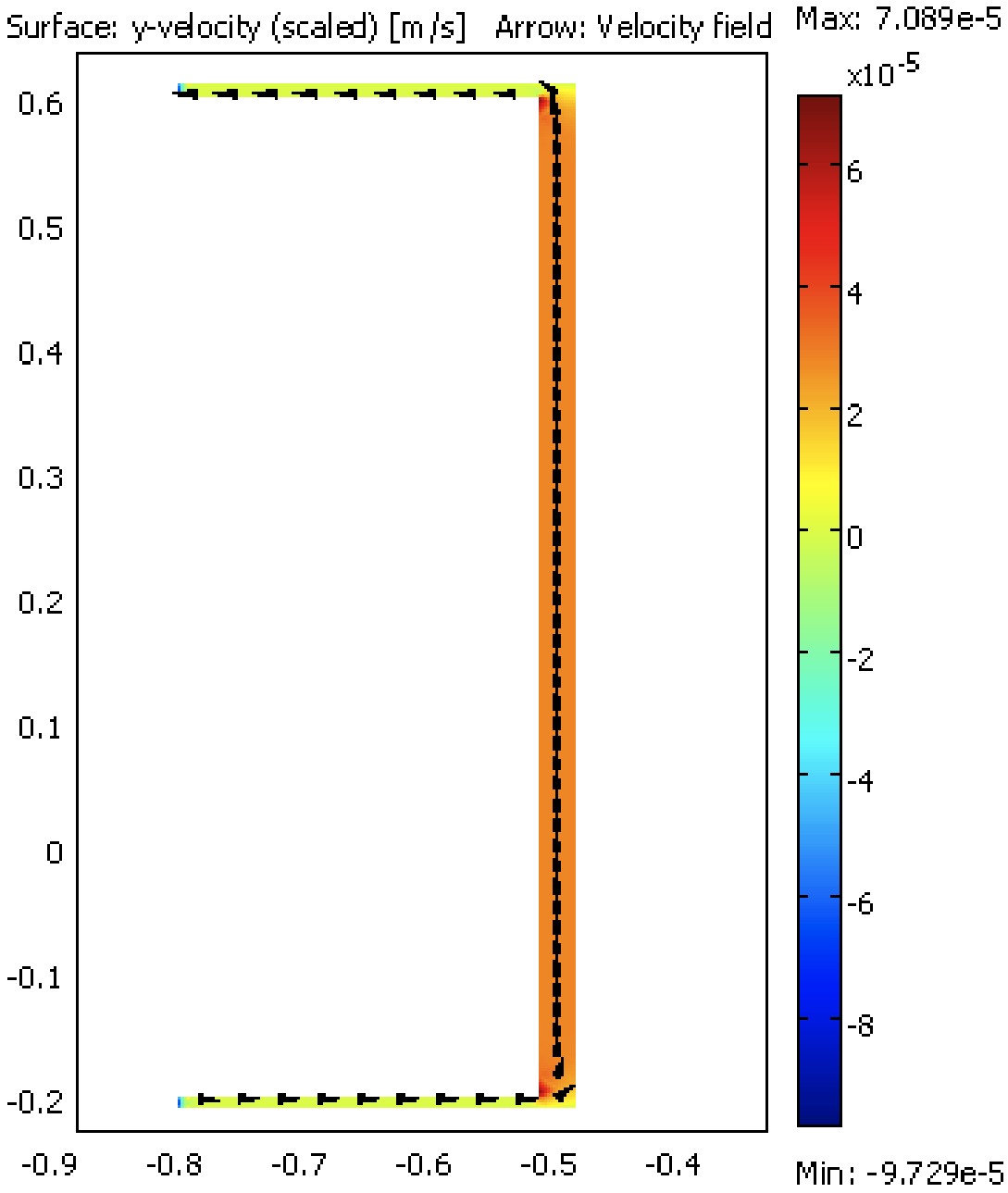

Figure 25: Frac 1.5 cm

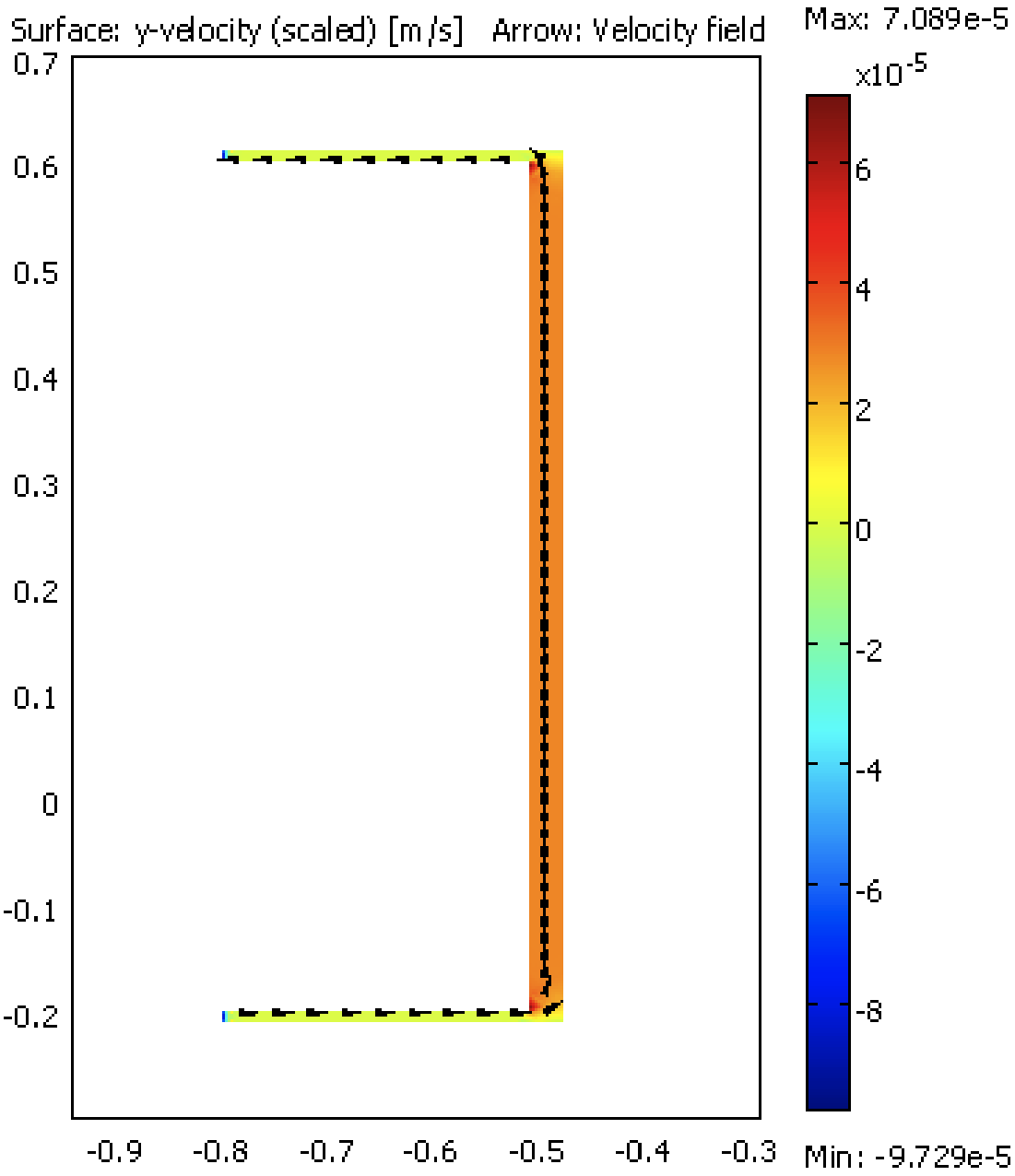

Figure 26: Frac 2.5 cm

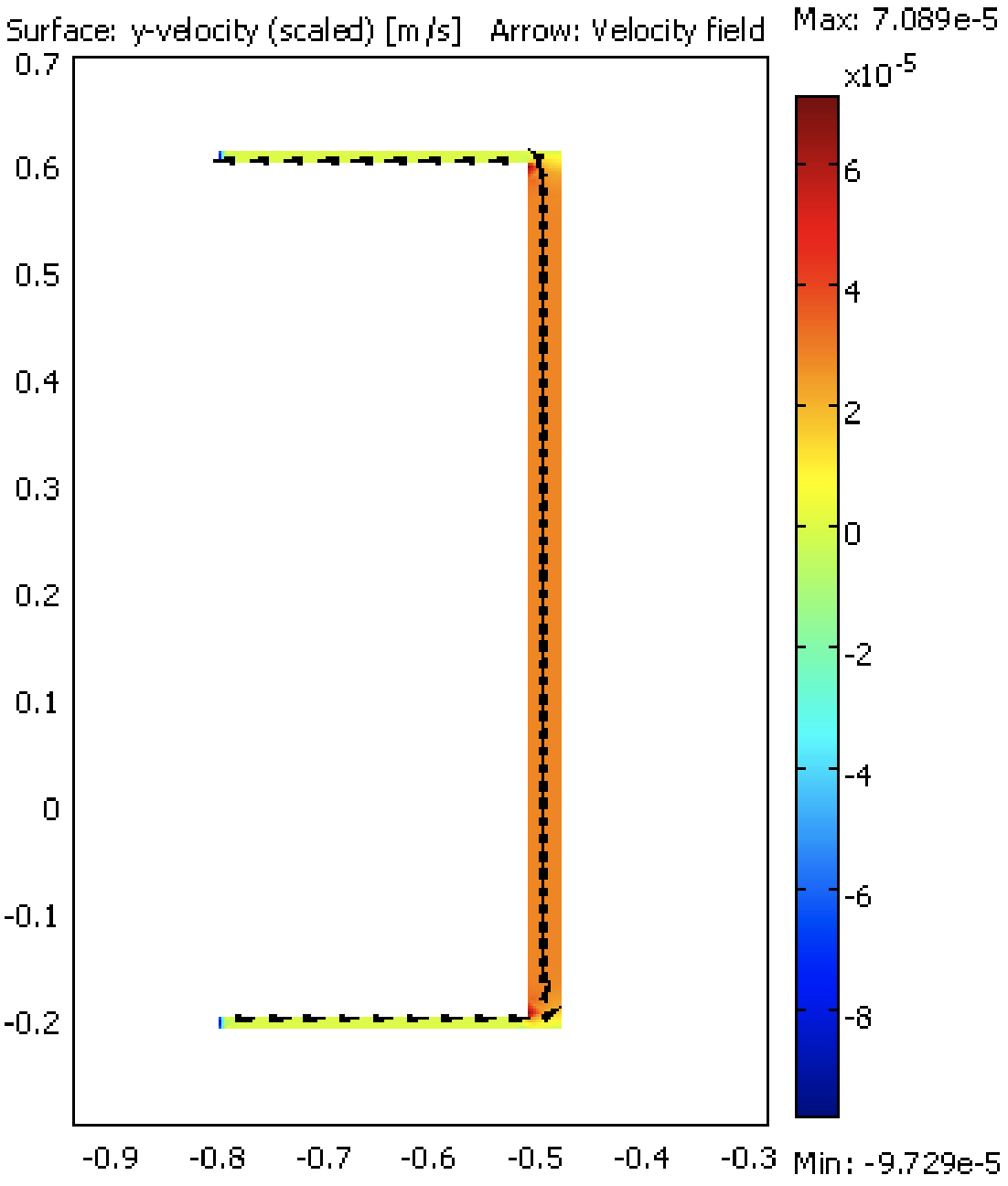

Figure 27: Frac 3 cm